PHYSICAL REVIEW B **85**, 024410 (2012)

Micromagnetic modeling and small-angle neutron scattering characterization of magnetic nanocomposites

Sergey Erokhin,[1] Dmitry Berkov,[1,*] Nataliya Gorn,[1] and Andreas Michels[2]
[1]*INNOVENT Technology Development, Jena, Germany*
[2]*Laboratory for the Physics of Advanced Materials, University of Luxembourg, Luxembourg*
(Received 5 September 2011; revised manuscript received 7 November 2011; published 11 January 2012)

A new methodology for micromagnetic simulations of magnetic nanocomposites is presented. The methodology is especially suitable for simulations of two-phase composites consisting of magnetically hard inclusions in a soft magnetic matrix phase. The proposed technique allows us to avoid unnecessary discretization of the "hard" inclusions (these are normally in a single-domain state) but enables arbitrary fine discretization of the "soft" phase. The method is applied to the determination of the equilibrium magnetization state of an iron-based nanocomposite from the Nanoperm (FeZrBCu) family of alloys and to the calculation of the corresponding small-angle neutron scattering (SANS) cross-section. The results of our simulations exhibit a remarkable agreement with nontrivial "clover-leaf" SANS cross-sections observed experimentally.

DOI: 10.1103/PhysRevB.85.024410 PACS number(s): 75.75.−c, 75.78.Cd, 75.25.−j, 75.50.Tt

I. INTRODUCTION

Magnetic nanocomposites are bulk materials that consist of magnetic nanocrystals embedded in an amorphous, usually magnetically soft phase (matrix). The growing interest in this class of magnetic materials is caused by their nontrivial magnetic properties, which are highly interesting from a fundamental point of view and for existing and potential applications of such nanocomposites. In particular, the magnetic microstructure in nanocrystalline ferromagnets can be highly inhomogeneous, which is mainly a consequence of the following two microstructural features. First, magnetic material parameters (saturation magnetization M_S, exchange-stiffness constant A, and anisotropy constant K) for the two constituent magnetic phases may be very different. Second, at each grain or phase boundary, the crystallographic anisotropy axes change their directions randomly, thus altering the locally preferred magnetization directions. In addition, new physical effects may be expected whenever the structural "correlation length" of the microstructure—in this case, the average grain size D—is reduced below a characteristic intrinsic magnetic length scale that is linked to the atomistic origin of magnetism (crossing length scales scenario). An outstanding example is the phenomenon of exchange softening[1] that is observed in Fe-based alloys whenever D becomes smaller than the so-called exchange correlation length $l_K \sim (A/K)^{(1/2)}$, which for Fe-based alloys is approximately 20–40 nm.

The inherently existing nonuniformity in the spin system leads to interesting magnetic properties of nanocrystalline magnets, which can be very different from the corresponding features of their coarser-grained (microcrystalline) counterparts. Famous examples for alloy development (based on the previously sketched rationales) include nanocrystalline NdFeB-based permanent magnets[2–5] or Fe-based alloys of the Finemet (Vitroperm), Hitperm, or Nanoperm type,[1,6,7] which are magnetically extremely soft and, due to their high permeability, are widely used as transformer cores and shielding material.

Downscaling of the individual nanosized building blocks places increasing demands on observational techniques to resolve ever-finer details of the magnetic microstructure. Most commonly used techniques, such as Kerr and Lorentz microscopy,[8] magnetic force microscopy,[9] spin-polarized scanning tunneling microscopy,[10,11] or photoelectron spectroscopy,[12] generally image the magnetic microstructure at the sample *surfaces*. In addition, to probe a structure from macroscopic dimensions down to the atomic scale, we must combine all of these techniques.

In contrast to the previously mentioned methods, magnetic small-angle neutron scattering (SANS) is probably the only technique capable of studying the spin distribution in the volume of a magnetic material *and* on a length scale from several nanometers up to a few hundreds of nanometers (for recent reviews of magnetic SANS, see Refs. 13–15).

Magnetic SANS is also a versatile technique, which allows us to investigate a range of materials, including ferrofluids, magnetic nanoparticles in a polymer matrix, magnetic recording media, colossal magnetoresistance materials, superconductors, spin glasses, amorphous metals, Invar alloys, magnetic single crystals, molten and solid elemental ferromagnets (Fe, Co, Ni, Tb, and Gd), nanowires, precipitates in steels, and diluted paramagnets in deuterated solutions.[13–19] Nanocomposite materials have been also extensively studied using SANS, whereby both magnetically hard[20,21] and soft[18,22–30] systems have been investigated, and a couple of interesting new results have been obtained. For instance, studies of FeSi-based nanocrystalline soft magnets by this technique have identified layers of reduced magnetization at the interfaces between the FeSi crystals and the surrounding amorphous matrix.[22–24] Also, a transition to a superparamagnetic behavior at the ordering temperature of the matrix phase was found.[26] Magnetic field–dependent SANS measurements, in combination with Kerr microscopy on magnetically textured FeSi-based ribbons,[27,28] have revealed the domain orientation and the characteristic length scale of intradomain spin misalignment.

In contrast to nuclear SANS, where the theoretical concepts are relatively well established,[31] understanding of magnetic SANS on bulk ferromagnets is still at its beginning. The main difficulty comes from a variety of competing interactions present in a ferromagnet. To analyze magnetic SANS data on

magnetic materials in general and in magnetic nanocomposites in particular, we should be able to calculate the corresponding equilibrium magnetization configuration. The most widely used mesoscopic theoretical approach for this purpose is the micromagnetic phenomenology,[32–34] in which four main contributions to the total magnetic free energy (external field, magnetocrystalline anisotropy, exchange, and magnetodipolar interaction energy) are taken into account. Determination of an equilibrium magnetization state of a ferromagnet using the micromagnetic framework amounts to the solution of a set of nonlinear partial differential equations, which cannot be done analytically in most practically relevant problems.

Therefore, closed-form expressions for the ensuing so-called spin-misalignment scattering cross-section are limited to the approach-to-saturation regime, in which the micromagnetic equations can be linearized. Pioneering work in this direction was carried out in Ref. 35, where the magnetic SANS cross-section arising from spin disorder due to dislocations in ferromagnetic metals was computed. The ansatz from Ref. 35 was generalized by Michels and Weissmüller,[15] who developed the theoretical framework for analyzing random-anisotropy–type nanocrystalline ferromagnets. However, the usefulness of these analytical theories is limited due to the difficulties mentioned previously.

A semianalytical model for the interpretation of SANS measurements on nanostructured simple metals presented in Ref. 36 assumes that the magnetic material consists of *spherical domains* embedded into a *homogeneously* magnetized matrix. The magnetization orientation inside each domain was determined, assuming that each domain possesses a uniaxial anisotropy with the value computed from the random-anisotropy model of Herzer[1,7] (domains were supposed to consist of several magnetically coupled grains). This (Stoner-Wohlfarth–type) model could explain qualitatively the evolution of the SANS intensity contours with the applied field in nanocrystalline Fe and Co. However, due to a simplified treatment of the interaction between the domains (neglecting, e.g., the magnetodipolar interaction) and between the domains and the matrix, this model cannot be applied to the physically most interesting case of an inhomogeneously magnetized matrix and thus is not suitable for quantitative studies of remagnetization processes in multiphase composites.

For this reason, full-scale numerical micromagnetic studies of magnetic SANS are clearly necessary. In the last decade, such simulations have become possible due to the steady increase in the computer power and due to the extensive development of micromagnetic software packages such as OOMMF,[37] LLG,[38] MicroMagus,[39] and MuMax.[40] For example, Ogrin *et al.*[41] used the OOMMF code to compute the magnetic SANS cross-section of CoCrPtB-based longitudinal recording media. Saranu *et al.*[42] utilized the same OOMMF tool to study the effect of the magnetostatic energy and average crystallite size on the magnetic SANS of nanocrystalline ferromagnets (see Sec. II for more details).

However, all of these commercially or freely available micromagnetic packages have serious drawbacks regarding the ability to simulate magnetization structures in bulk magnetic nanocomposites, as explained in detail in Sec. II. For this reason, simulations of the magnetization distribution in composite system of practical interest have been hardly possible up to now,[43–45] so a new methodology for micromagnetic studies of nanocomposites is required. Having such a methodology at our disposal would allow better understanding of equilibrium magnetization states and magnetization dynamics in nanocomposites and deeper interpretation of corresponding results obtained via magnetic SANS. This paper is devoted to the development of such a methodology and to the analysis of some nontrivial cross-section patterns observed recently in alloys of the Nanoperm type.[18]

The paper is organized as follows: In Sec. II, we explain why the two main classes of existing micromagnetic methods are not suitable for simulations of hard–soft nanocomposites. In Sec. III, we discuss our new methodology, describing the mesh-generating algorithm and the evaluation of the energy contributions, and present the results of analytical and numerical tests of our code. Sec. IV starts with our simulation results for equilibrium magnetization configurations in nanocomposites of the Nanoperm type. Then we compare in detail magnetic SANS cross-sections calculated numerically from these equilibrium magnetization configurations with those observed experimentally in Ref. 18. Sec. V summarizes the main results obtained in this study.

II. NONAPPLICABILITY OF EXISTING NUMERICAL MICROMAGNETIC METHODS

Micromagnetics is a mesoscopic phenomenological theory that allows—in its quasistatic version—us to determine the equilibrium magnetization configuration of a ferromagnetic body when the applied field, the geometry of the ferromagnet, and its magnetic material parameters are known.[32–34] For this purpose, the total magnetic free energy of a ferromagnet (which contains, in the most common case, contributions from energy due to an external field, exchange, anisotropy, and magnetodipolar interaction energies) is minimized. Mainly due to the nonlocality of the magnetodipolar energy, most practically interesting tasks cannot be solved analytically, so numerical simulations should be carried out. At present, numerical micromagnetics is a large and continuously expanding research field, which has been extensively reviewed, e.g., in a recent handbook.[46] Thus, in this subsection, we briefly discuss only methodological details relevant for numerical simulations of nanocomposite materials.

Such materials are probably the most complicated objects from the point of view of numerical simulations, because they consist of at least two phases with nonflat boundaries between them—a typical example is a hard–soft nanocomposite "made of" magnetically hard grains surrounded by a soft (but also ferromagnetic) matrix. Such a system is difficult to simulate for the following reasons.

All micromagnetic simulation methods can be roughly divided into two classes: finite-difference and finite-element algorithms.[46] In the former methods, the system under study is discretized into a regular (usually rectangular) grid. Such a grid allows the usage of simple finite-difference formulas for the exchange field calculation, which in the continuous formulation is the differential operator acting on the magnetization field $\mathbf{M}(\mathbf{x})$. In addition, the translational invariance of a regular grid enables the application of the fast Fourier transformation (FFT) for the evaluation of the magnetodipolar interaction field

(energy). For a system discretized into N finite elements, the FFT technique reduces the operation count for this nonlocal interaction from $\sim N^2$ to $\sim N \log N$. The disadvantage of a regular grid is a pure approximation for the curved boundaries. This is a serious drawback for simulations of nanocomposites, where the accurate representation of the interphase boundaries (and associated exchange and magnetodipolar effects) is crucially important for a proper system description.

The second group of numerical micromagnetic methods (finite-element methods) employs the discretization of the studied body into tetrahedrons of arbitrary shapes and sizes. Such flexible discretization allows for a quite accurate representation of curved boundaries, including those between magnetically hard inclusions and a soft matrix. The tributes to pay for this convenience are (1) complicated methods for the evaluation of the exchange field (requires a representation of a differential operator on an irregular lattice) and (2) the impossibility to use FFT for the computation of the magnetodipolar field. This forces the usage of highly complicated methods for the calculation of this field, based on the decomposition of the scalar or vector magnetic potentials and the solution of corresponding Poisson equations for these potentials on an irregular grid.[46] This technique can be applied to systems with open boundary conditions only, resulting in another limitation of the finite-element method: periodic boundary conditions (which are routinely applied in simulations of bulk materials to eliminate strong finite-size effects) cannot be used. The impossibility of using periodic boundary conditions is a serious disadvantage when simulating SANS experiments on nanocomposites (whereby the scattering intensity is sensitive to magnetization fluctuations in the *bulk*), because surface demagnetizing effects might be significant due to (1) a substantial volume fraction occupied by a soft ferromagnetic or superparamagnetic nanocomposite matrix and (2) a relatively small simulation volume affordable even for modern computers.

Another unfavorable feature of tetrahedral discretization is the necessity of discretizing into tetrahedrons the hard magnetic grains, even when it is clear that the magnetization configuration within a single grain is nearly collinear. This leads to a significant increase in the number of finite elements and in a corresponding increase in computation time (see Ref. 47 for a corresponding discussion and a suggestion of how this problem might be solved in frames of the finite-element method).

For the reasons explained previously, micromagnetic modeling of SANS experiments on nanocomposites is rare. Full-scale micromagnetic simulations of SANS measurements on a two-phase system were reported recently in Ref. 41, where the authors modeled the magnetization structure of a longitudinal magnetic recording media film. Based on experimental characterization of such media, Ogrin *et al.*[41] built a two-phase model of magnetic grains consisting of a magnetically hard grain core and an essentially paramagnetic shell (although with a very high susceptibility). The authors used the OOMMF code, employing the standard finite-difference scheme, so a very fine discretization grid ($0.3 \times 0.3 \times 0.3$ nm^3 cells) was necessary to reproduce the spherical shape of grain cores with significant accuracy. Thus, only a limited number of grains ($\sim$50) could be simulated. In addition, the exchange interaction between the grains and within the matrix (representing by the merging grain shells) was neglected. Under these simplifying assumptions and using several adjustable parameters, the authors could achieve satisfactory agreement of the simulated SANS intensity profile with experimental data, showing great potential of micromagnetic simulations for interpreting the SANS experiments.

The overview presented here clearly shows that further numerical studies—including the development of new simulation methods—in this direction are highly desirable.

III. NEW MICROMAGNETIC METHODOLOGY

A. Mesh generation

For numerical simulations of two-phase nanocomposites described previously, we aim to generate a polyhedron mesh with the following properties: (1) it should allow us to represent each hard nanocrystallite as a single finite element, because the magnetization inside such a hard grain is nearly homogeneous; (2) the mesh should allow an arbitrary fine discretization of the soft magnetic matrix; and (3) the shape of meshing polyhedrons should be as close as possible to the spherical one to ensure a good-quality dipolar approximation for the calculation of the magnetodipolar interaction energy.

A mesh of polyhedral finite elements satisfying these requirements can be generated using two kinds of methods. The first group of methods employs various modifications of a purely geometric iterative algorithm, suggested in Ref. 48, for obtaining the random close packing of hard spheres. The initial distribution of sphere centers is random. At each step, the worst overlap of two spheres is eliminated by moving these spheres along the line connecting their centers until these spheres are separated. This procedure may introduce new overlaps, but they are eliminated during the next steps so that the packing quality improves (on average). The algorithm is robust and produces the random close packing of nonoverlapping spheres with any desired accuracy (see Ref. 48 for details). Unfortunately, the computation time for this method is $\sim N^2$, where N is the number of elements, so the maximal number of spheres that can be positioned by this method within a reasonable computation time is $N \approx 10^4$.

To generate a mesh with a much larger number of elements ($N > 10^5$), we developed a "physical" algorithm, which is based on the model of spheres interacting via the short-range repulsive potential

$$U_i = \sum_{j=1}^{N} A_{\text{pot}} \exp\left\{-\frac{d_{ij} - (r_i + r_j)}{r_{\text{dec}}}\right\}, \qquad (1)$$

where A_{pot} is a constant (in a typical case, $A_{\text{pot}} = 10$), d_{ij} is the distance between the centers of interacting spheres with radii r_i and r_j, and r_{dec} is the interaction decay radius. Again, at the beginning of the iteration procedure, we position the sphere centers randomly. Then we move these spheres according to the dissipative equation of motion resulting from the forces derived from their interaction in Eq. (1). The time step for the integration of the corresponding equation of motion is adjusted so that the total system energy decreases after each step. This procedure also leads to the decrease of overlaps between the spheres due to the repulsive nature of the potential in Eq. (1).

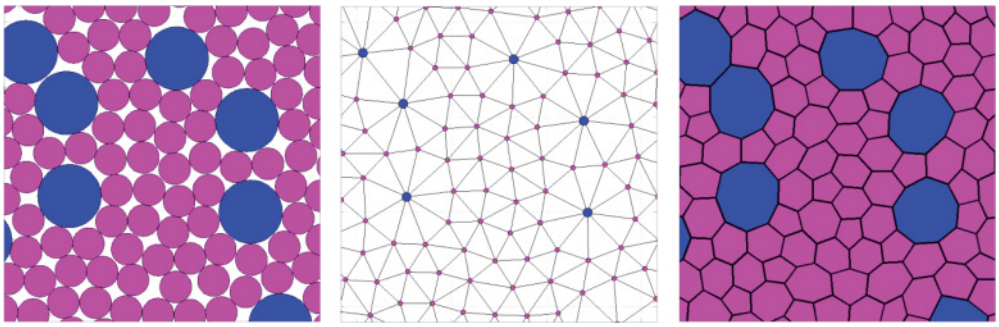

FIG. 1. (Color online) The algorithm for the mesh generation: (a) Random close packing of spheres with different diameters (large spheres correspond to the magnetically hard inclusions), (b) sphere centers used as location points for magnetic moments, and (c) discretization of the system into the Voronoi polyhedrons corresponding to the triangulation shown in (b); these polyhedrons might be considered finite elements used for system discretization.

We continue to move the spheres until the maximum overlap between them does not exceed the prescribed small value (we tested whether for our purposes the minimal remaining overlap of $(r_i + r_j)/d_{ij} > 0.95$ is good enough). Various possibilities exist to increase the efficiency of this algorithm. In particular, we might decrease the decay radius of the potential r_{dec} (thus making the potential harder) when overlapping between spheres decreases during sphere motion. A typical two-dimensional (2D) example of the configuration obtained this way is shown in Fig. 1(a). Because of the random spatial arrangement of spheres obtained this way, we avoid possible artifacts caused by the regular placement of finite elements.

After the spheres have been positioned using one of the two algorithms described previously, their centers [Fig. 1(b)] are used as location points of magnetic dipoles. To compute the magnitudes μ_i of these dipoles, we first multiply the volume of the corresponding sphere by the saturation magnetization of that material inside which the dipole is located (nanocomposites consist of materials with different magnetization). Second, we take into account that even the closely packed spheres do not fill the entire sample volume, occupying only a certain volume fraction c_{vol} (approximately 55% for a typical configuration) of the available space. For this reason, we divide the magnitude of each dipole by this volume fraction so that finally $\mu_i = (4\pi M_S/3c_{\text{vol}})r_i^3$, ensuring that in the saturated state the total magnetic moment of the discretized system is the same as that of the initial continuous system.

The whole algorithm can be viewed as a method to discretize a sample into polyhedrons [Fig. 1(c)] with a nearly spherical shape, because they "inherit" the spatial structure obtained by positioning of closely packed spheres. The shape of the volume that is "occupied" by each magnetic moment is nearly spherical, allowing us to use the dipolar approximation by evaluation of the magnetodipolar interaction between the moments.

Finally, both algorithms allow the usage of polyhedrons of different sizes if we need different meshing on different system locations.

B. Evaluation of energy contributions and energy minimization

In our model, we take into account the four standard contributions to the total magnetic energy: system energy in the external field, magnetic anisotropy, exchange, and magnetodipolar interaction energies.

1. External field and anisotropy energies

The external field and anisotropy energies (uniaxial and/or cubic) are calculated in our model in the usual way, i.e.,

$$E_{\text{ext}} = -\sum_{i=1}^{N} \boldsymbol{\mu}_i \mathbf{H}_{\text{ext}} \tag{2}$$

$$E_{\text{an}}^{\text{un}} = -\sum_{i=1}^{N} K_i^{\text{un}} V_i (\mathbf{m}_i \mathbf{n}_i)^2 \tag{3}$$

$$E_{\text{an}}^{\text{cub}} = \sum_{i=1}^{N} K_i^{\text{cub}} V_i \left(m_{i,x'}^2 m_{i,y'}^2 + m_{i,y'}^2 m_{i,z'}^2 + m_{i,x'}^2 m_{i,z'}^2 \right) \tag{4}$$

where $\mathbf{H}_{\text{ext}}$ is the external field; $\boldsymbol{\mu}_i$ and V_i are the magnetic moment and the volume of the ith element, respectively; and $\mathbf{m}_i$ is the unit magnetization vector. Both the anisotropy constants K_i and the directions of the anisotropy axes $\mathbf{n}_i$ are site dependent, as needed for a polycrystalline material. In the case of cubic anisotropy, the symbols $m_{x'}$, etc., mean the components of unit magnetization vectors in the local coordinate system (attached to the cubic anisotropy axes).

2. Exchange energy

For the exchange energy evaluation, we use the nearest-neighbor approximation. The continuous integral version of this energy employs the magnetization gradients

$$E_{\text{exch}} = \int_V A(\mathbf{r})[(\nabla m_x)^2 + (\nabla m_y)^2 + (\nabla m_z)^2] dV. \tag{5}$$

For a regular cubic grid with the cell size a (and the cell volume $\Delta V = a^3$), it can be shown rigorously (see the detailed proof in Ref. 49) that the integral in Eq. (5) can be approximated as the sum

$$E_{\text{exch}} = -\frac{1}{2} \sum_{i=1}^{N} \sum_{j \subset n.n.(i)} \frac{2A_{ij}\Delta V}{a^2} (\mathbf{m}_i \mathbf{m}_j). \tag{6a}$$

Here, A_{ij} denotes the exchange constant between cells i and j, and the notation $j \subset n.n.(i)$ means that summation in the inner sum is performed over the nearest neighbors of cell i.

(This Heisenberg-like expression is valid only when the angles between neighboring moments are not too large.[49]) However, we use a disordered system of finite elements that has different volumes, different distances between the element centers, and different numbers of nearest neighbors for each element, so the expression in Eq. (6a) cannot be used.

The straightforward way to compute the exchange interaction in our case is to employ a rigorous general formula suitable for the evaluation of the integral in Eq. (5) for a system, where the values of the integrand (magnetization vectors **m**) are known at arbitrarily distributed spatial points. Such a formula amounts to approximation of the vector function $\mathbf{m}(\mathbf{r})$ using some polynomial interpolation of this function between the points where $\mathbf{m}(\mathbf{r})$ is defined. Since the integrand in Eq. (5) includes first spatial derivatives of the magnetization field, corresponding polynomials should deliver a continuous (and better, smooth) first derivative of $\mathbf{m}(\mathbf{r})$. In addition, keeping in mind that the condition $|\mathbf{m}(\mathbf{r})| = 1$ must be fulfilled everywhere, we should use interpolation of magnetization angles rather than that of Cartesian components of **m**. Both features would lead to a highly complicated algorithm for exchange energy evaluation that is subject to serious stability problems.

Therefore, we decided to modify the expression in Eq. (6a) to account in a simpler way for the differences between a regular grid and a disordered system as mentioned previously. First, following the derivation of the expression in Eq. (6a) presented in Ref. 49, the volume ΔV in the numerator is not the volume of the cubic discretization cell but the volume enclosed between the centers of cell i and neighboring cell j (for a rectangular lattice, this volume is equal to the cell volume, because it includes two halves of identical rectangular cells). Therefore, for a disordered system, ΔV should be replaced by $\bar{V}_{ij} = (V_i + V_j)/2$, where V_i and V_j are the volumes of the ith and jth finite elements, respectively.

The second necessary correction is replacement of the distance a between the cell centers in a cubical lattice (in the denominator) by the distance Δr_{ij} between the centers of cells i and j.

The third—and most nontrivial—issue is due to the following principal difference between the lattice geometries of a rectangular and those of a disordered lattice. In a rectangular lattice, each cell has exactly $N_{\mathrm{nn}} = 6$ nearest neighbors, and the angles between the directions from the cell center toward its neighbors in x-, y-, and z-directions are always 90°. Hence, the overlapping of the volumes enclosed between the centers of neighboring cells in, say, x- and y-directions is always the same and is already taken into account by the derivation in Eq. (6a) (this overlapping should not be confused with the overlapping of spheres in the construction of our disordered mesh in Sec. III A). In contrast to this feature of a rectangular lattice, for a disordered system of finite elements (polyhedra), the number of nearest neighbors may vary for different finite elements and the overlapping of volumes enclosed between the center of a given cell and the centers of its different neighbors may also be different. For example, if some particular element has more than six nearest neighbors, then the volumes enclosed between its center and the centers of its different neighbors would overlap more than for a rectangular lattice. In this case, the exchange energy evaluated using a sum in Eq. (6a)—even with the two corrections explained previously—would be overestimated due to this excessive overlapping.

The simplest method to avoid this artifact is the introduction of the correction factor $6/n_{\mathrm{av}}$, where n_{av} is the average number of nearest neighbors for the given realization of our disordered system. This way, we account for the effect of the incorrect count of the overlapping regions mentioned previously. The accuracy of the expression corrected using this simple factor cannot be estimated in advance, but both the tests presented in Ref. 54 and the additional tests discussed in Sec. III.C show that—taking into account its simplicity—the accuracy achieved by this correction is surprisingly good.

Summarizing, for magnetic moments belonging to the same phase, we used the following modified form of the Heisenberg-like expression for the nearest-neighbor exchange:

$$E_{\mathrm{exch}} = -\frac{1}{2}\sum_{i=1}^{N}\sum_{j\subset n.n.(i)}\frac{2A_{ij}\bar{V}_{ij}}{\Delta r_{ij}^2}(\mathbf{m}_i\mathbf{m}_j), \tag{6b}$$

where, as mentioned previously, $\bar{V}_{ij} = (V_i + V_j)/2$, Δr_{ij} is the distance between the dipoles i and j belonging to elements with volumes V_i and V_j, and A_{ij} is the exchange constant.

The last point to be discussed is the choice of nearest neighbors, which should be used in the inner sum in Eq. (6b). The definition of these neighbors is not unambiguous in disordered systems. We adopted the convention that two magnetic moments are considered nearest neighbors if they are separated by a distance no larger than $d_{\max} = 1.4 \cdot (r_i + r_j)$. The cutoff factor (1.4) is chosen so that for the overwhelming majority of finite elements, the two that have a common face [when they are considered polyhedra; see Fig. 1(c)] are treated as nearest neighbors.

To describe the exchange between the two finite elements (polyhedrons) belonging to different phases (hard and soft), we use another formula for their exchange interaction:

$$E_{\mathrm{ex}} = -\frac{1}{2}\sum_{i=1}^{N}\sum_{\langle j,i\rangle}\frac{2A_{ij}(V_{\mathrm{sp}}/2)}{(\Delta r_{ij} - R_{\mathrm{hp}})^2}(\mathbf{m}_i\mathbf{m}_j). \tag{7}$$

Here, V_{sp} is the volume of a soft phase element, and R_{hp} is the radius of the sphere corresponding to the hard phase element. The expression in Eq. (7) accounts for, in this case, the magnetization rotation occurring almost entirely within the polyhedron corresponding to the soft phase.

3. *Magnetodipolar interaction energy*

The last energy term—energy of the magnetodipolar interaction between the moments and the corresponding contribution to the total effective field—is computed in the dipolar approximation as

$$E_{\mathrm{dip}} = -\frac{1}{2}\sum_{i=1}^{N}\boldsymbol{\mu}_i\sum_{j\neq i}\frac{3\mathbf{e}_{ij}(\mathbf{e}_{ij}\boldsymbol{\mu}_j) - \boldsymbol{\mu}_j}{\Delta r_{ij}^3}; \tag{8}$$

i.e., magnetic moments of finite elements are treated as point dipoles located in the centers of generated, closely packed spheres (see the earlier discussion). This approximation would be exact only for spherical finite elements. Hence, it results in some computational errors for our discretized system, which should be considered, strictly speaking, as composed of finite

elements in the form of polyhedrons [as shown schematically in Fig. 1(c)]. However, these errors are small, because the shape of our finite elements is close to spherical due to the special algorithm employed for the generation of magnetic moment location points.

The summation in Eq. (8) is performed by the so-called particle-mesh Ewald method. A didactically detailed general introduction to Ewald methods can be found in Ref. 50. The corresponding specific implementation for the magnetodipolar interaction for lattice-based and disordered systems of magnetic particles is described in our papers.[51,52] The lattice Ewald method for disordered systems consists of the following stages: (1) mapping of magnetic moments of the initial (disordered) system onto a rectangular lattice, (2) evaluation of the magnetodipolar field for the translationally invariant system obtained this way using the standard lattice Ewald method, and (3) backward interpolation of the field obtained on the rectangular grid in the previous step onto the initial positions of magnetic dipoles. The most time-consuming step (2) can be performed using the FFT technique—due to the presence of a translationally invariant grid—which allows us to reduce the operation count from N^2 (for the standard Ewald method) to $N \cdot \log(N)$. Hence, simulations of systems consisting of $N \sim 10^5 - 10^6$ moments become possible.

The major sources of errors in the method are the mapping of the initial disordered system onto a rectangular grid and the backinterpolation of the magnetodipolar field (errors for the properly implemented lattice Ewald method are vanishingly small). However, these errors may be reduced below the desired threshold by the proper choice of mapping scheme (see Ref. 53 for a detailed description). We found that if we choose the lattice constant equal to the radius of the smallest spheres used for the mesh generation, then the usage of the linear mapping scheme, together with the separate evaluation of the nearest-neighbor contribution, ensures that corresponding errors are less than 1%.

To minimize the total magnetic energy, obtained as the sum of all contributions discussed previously, we used the simplified gradient method, employing the dissipation term in the Landau-Lifshitz equation of motion for magnetic moments.[46] This means that the magnetization configuration at each step is updated according to the rule

$$\mathbf{m}_i^{\text{new}} = \mathbf{m}_i^{\text{old}} - \Delta t\left[\mathbf{m}_i^{\text{old}} \times \left[\mathbf{m}_i^{\text{old}} \times \mathbf{h}_i^{\text{eff}}\right]\right], \qquad (9)$$

where $\mathbf{m}_i$ denotes the unit magnetization vector $\mathbf{m}_i = \mathbf{M}_i/M_S$ and $\mathbf{h}_i^{\text{eff}} = \mathbf{H}_i^{\text{eff}}/M_S$ is the reduced effective field $\mathbf{H}_i^{\text{eff}}$, evaluated in a standard way as the negative derivative of the total energy over the magnetic moment projections.[46]

Since we are looking for the energy minimum, the time step choice in Eq. (9) is based on monitoring of the total energy: if after the iteration step the total energy decreased, we accept this step. If the energy increased, we restore the previous magnetization state, halve the time step ($\Delta t \rightarrow \Delta t/2$), and repeat the iteration. To avoid unnecessary small time steps, we used a simple adaptive step size control: the time step is doubled if the last few steps (typically 5–10 steps) were successful. The minimization process is terminated if the maximal torque acting on magnetic moments is sufficiently small: $\max_{\{i\}} |[\mathbf{m}_i \times \mathbf{h}_i^{\text{eff}}]| < \varepsilon$ (this condition is more sensitive than the often-used criterion of the energy difference between the two subsequent steps). We found that in all tested cases, the value $\varepsilon = 10^{-4}$ was small enough to ensure the convergence of the minimization procedure.

C. Numerical tests of the new methodology

The methodology explained previously was already tested on two example problems (see the brief report in Ref. 54). First, we reproduced with high accuracy the analytically known magnetization profile for a standard three-dimensional (3D) Bloch wall. Second, for a trial 3D magnetic configuration defined via some simple trigonometric functions of coordinates (to ensure smooth spatial variations of the system magnetization), we obtained good agreement between the energy values found by the new method and the micromagnetic package MicroMagus,[39] which employs standard finite-difference formalism.

In this paper, we present two additional tests in which we compare the equilibrium magnetization configurations of a cubic magnetic particle, obtained also via our new method, and the MicroMagus package. The particle size was chosen to be $40 \times 40 \times 40$ nm^3, saturation magnetization was set to $M_S = 800$ G, the exchange constant was $A = 1 \times 10^{-6}$ erg/cm, and the uniaxial anisotropy constant was $K = 5 \times 10^5$ erg/cm^3. For application of the new method, the cube was discretized (using the algorithm described previously) into $N = 9000$ elements with the typical size $d = 2$ nm. For the standard finite difference simulations, a cell size of $2.5 \times 2.5 \times 2.5$ nm^2 was used.

For the tests, we chose two magnetization configurations that are typical for particles of this size: the vortex state and the so-called flower state. To obtain the vortex state, we started the minimization procedure from the magnetization state that is topologically equivalent to the vortex—the so-called closed Landau domain configuration. The flower state was obtained by starting the energy minimization from the homogenous configuration, with magnetization directed along one of the cube sides.

Comparison of energies for the equilibrium magnetization states (Fig. 2) obtained by the new method and the standard finite difference simulations (MicroMagus package) is presented in Table I. The energies obtained by both methods agree well. The only energy exhibiting a significant relative difference is the anisotropy energy for the flower state; however, this significant relative difference ($\Delta E/E$) arises simply due to a very low value of this energy. In all, agreement between the new and the established methodologies for all cases in which the standard methods are applicable are fully satisfactory.

IV. SIMULATIONS OF MAGNETIZATION PROCESSES AND MAGNETIC SANS IMAGES FOR NANOCOMPOSITES

A. Simulation of magnetization processes

To study the micromagnetic properties of nanocomposites, we first performed simulations of magnetization processes for a two-phase model system. This system should imitate the Nanoperm composite studied in Ref. 18, where the hard phase consisted of Fe precipitates with the average size

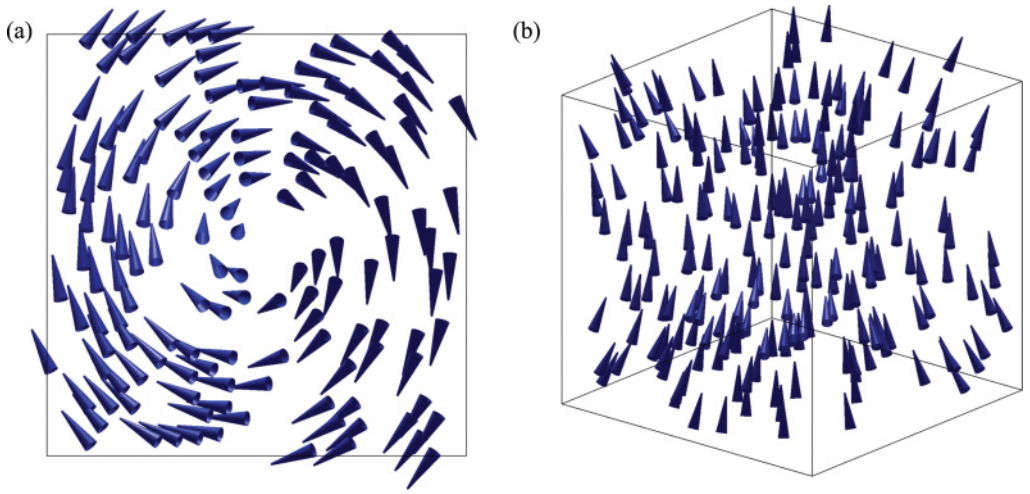

FIG. 2. (Color online) (a) Vortex (2D cross-section) and (b) flower (3D plot) magnetization configurations obtained by the new method explained in Sec. III.A and III.B.

$D_{\text{hard}} = 12$ nm and the volume fraction of precipitates $c_{\text{hard}} \approx 40\%$. For this reason, we chose by the mesh generation algorithm spheres with the diameter $D_{\text{lr}} = 10$ nm for the representation of magnetically hard grains and spheres with the much smaller diameter $D_{\text{sm}} = 5$ nm to discretize the soft matrix (D_{lr} is chosen to be somewhat smaller than D_{hard}, because the distance between the centers of spheres, generated as explained in Sec. III A, is on average somewhat larger than the sum of their radii). An example of the generated mesh is shown in Fig. 5. Furthermore, we used the following magnetic parameters for hard and soft phases: magnetizations $M_{\text{hard}} = 1750$ G (as for bulk Fe) and $M_{\text{soft}} = 550$ G (calculated from the average saturation magnetization of the material and parameters of Fe crystallites), as well as anisotropy constants $K_{\text{hard}} = 4.6 \times 10^5$ erg/cm^3 (also a typical value for bulk Fe) and $K_{\text{soft}} = 1.0 \times 10^3$ erg/cm^3 (the matrix is supposed to be nearly amorphous).

The problem of how to choose the exchange stiffness constants is addressed in detail here. For the example shown in Fig. 3, we set $A = 1.0 \times 10^{-8}$ erg/cm both for the interaction within the soft phase and between the hard and the soft phases. The magnetization direction is assumed to be constant within a single Fe grain, so there is no need to choose A for the hard phase. Such a low value of the exchange constant was used to increase the saturation field value and to make the relation between the crystalline and the magnetic microstructures more evident.

The size of the simulated system (rectangular box) was set to $125 \times 380 \times 380$ nm^3, which was discretized into $N = 10^5$ elements. Periodic boundary conditions were applied to avoid the effect of the stray field from the system borders.

The simulated magnetization curve, together with color images visualizing the evolution of the spatial magnetization configuration, is shown in Fig. 3(a). The color coding represents magnetic moment directions in the image plane as shown on the color wheel at the right of the panel (red on the right side of the wheel corresponds to the magnetization along the applied field and green on the wheel's left side corresponds to the opposite direction).

An important feature of the simulated magnetization process is the strong correlation between the system microstructure and the local magnetization direction. In Fig. 3(a), (in fields far from saturation) substantial magnetization deviations from the applied field direction occur where the hard phase grains are located. This correlation is evident from the comparison of locations of hard inclusions (shown by dark blue spots in the right inset at the bottom of the panel), with areas on the left inset where the magnetization substantially deviates from the field direction - visible as light (yellow) or dark (blue) spots.

A more detailed picture (on the length scale comparable to the average size of hard magnetic grains) of the local magnetization configuration obtained near saturation is shown in Fig. 3(b). This image shows that magnetic moments within the

TABLE I. Comparison of energies and reduced magnetizations (last row) for the vortex and flower magnetization states by the new method and the standard finite difference simulations (MicroMagus software).

	Vortex energies ($\times 10^{-11}$ erg)		Flower energies ($\times 10^{-11}$ erg)	
	New method	MicroMagus	New method	MicroMagus
E_{tot}	8.225	8.270	7.813	7.843
E_{an}	1.361	1.385	0.137	0.127
E_{exch}	4.409	4.562	0.434	0.441
E_{dem}	2.455	2.324	7.242	7.275
M/M_S	0.400	0.406	0.972	0.974

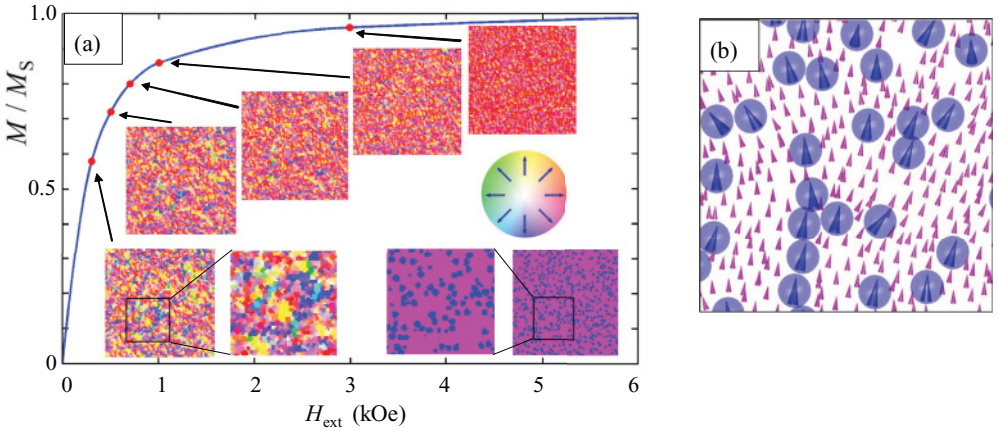

FIG. 3. (Color online) (a) Magnetization curve of a nanocomposite, together with the color images representing the magnetization states displayed for the cross-section through a 3D simulation volume. The inset in the lower right corner shows in blue squares the locations of the hard inclusions that clearly correlate with the magnetization deviations from the external field direction (inset in the lower left corner). (b) Magnetization state of the system near saturation displayed on the scale comparable to the size of a hard magnetic inclusion (see text for discussion).

soft phase roughly follow the directions of magnetic moments of hard inclusions—mainly due to the exchange interaction between the phases. The influence of the magnetodipolar interaction (which, as discussed later, is responsible for the appearance of a "clover-leaf" pattern) is too weak to be visible without averaging over a sufficiently large volume that includes many hard inclusions.

As mentioned previously, an important parameter is the exchange stiffness constant inside the soft phase and for the soft–hard phase exchange. This parameter can vary in a wide region, because it strongly depends on the concentration of iron atoms in the soft phase. Unfortunately, independent measurements of the exchange constant in the soft phase are not available. A rough estimation of the exchange constant in Nanoperm ($Fe_{89}Zr_7B_3Cu$) can be done using the Curie temperatures of the similar alloy $Fe_{91}Zr_7B_2$[55] and of body-centered cubic (bcc) iron:

$$A_{\mathrm{Np}} \sim A_{\mathrm{Fe}} \cdot \frac{T_c^{\mathrm{Np}}}{T_c^{\mathrm{Fe}}} \approx 2.5 \cdot 10^{-6}\mathrm{erg/cm} \cdot \frac{370\mathrm{K}}{1000\mathrm{K}} \approx 0.9 \cdot 10^{-6}\mathrm{erg/cm}$$

(we used the literature value $A_{\mathrm{Fe}} \approx 2.5 \times 10^{-6}$ erg/cm for the exchange constant of bcc Fe, which was computed from the data given in Ref. 56).

In addition, we simulated the dependence of the magnetization curves on this exchange constant. In principle, corresponding results could be used to establish the value of A by comparing simulated curves with those measured experimentally. Simulations were performed for the following exchange values: $A = 2.5 \times 10^{-6}$, 1.0×10^{-6}, 0.5×10^{-6}, and 0.1×10^{-6} erg/cm for exchange interactions both within the soft phase and between the hard and the soft phases, as well as without exchange interaction. Simulation results are presented in Fig. 4. Each point is the result of averaging over two to eight independent realizations of the configuration of finite elements with parameters listed previously. With increasing A, the system saturates faster (the saturation field strongly decreases), as it should be for a system consisting of random on-site anisotropy particles interacting via a ferromagnetic exchange that is mediated by a nearly amorphous matrix. A meaningful quantitative comparison of our results with the experimental magnetization curve presented in Ref. 18 is not possible yet, because the latter contains a strong paramagnetic-type contribution (probably from the small Fe clusters in the amorphous phase) not included in our numerical model. For comparison of our micromagnetic simulation results with experimental neutron-scattering data (described later), we used the value $A = 0.5 \times 10^{-6}$ erg/cm, which provides the best agreement with the experimental data.

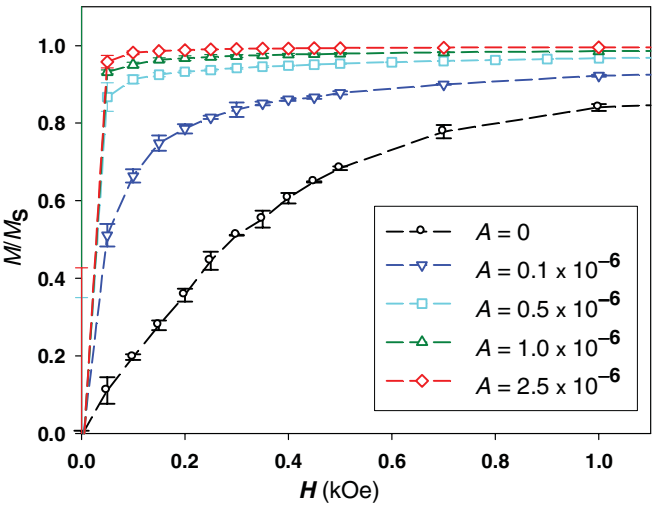

FIG. 4. (Color online) Magnetization curves for different exchange constants A for the soft phase (equal to the exchange constant applied for the interaction between the soft and the hard phases). Increase in the exchange constant leads to rapid decrease of the saturating field value.

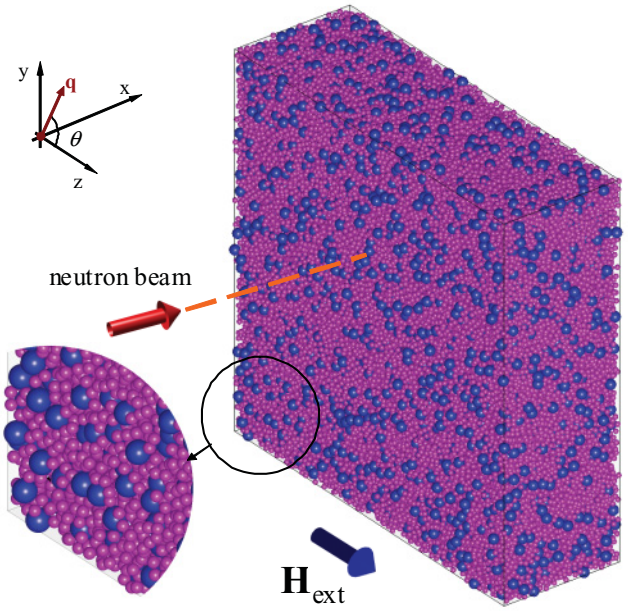

FIG. 5. (Color online) Geometry of the neutron scattering experiment used in simulations, together with the microscopic structure of the nanocomposite generated by the algorithm described in Sec. III.A (blue spheres correspond to magnetically hard grains).

B. Calculation of the SANS cross-section

Most SANS experiments rely on scattering geometry, where the applied magnetic field **H** is perpendicular to the wave vector $\mathbf{k}_0$ of the incident neutron beam (Fig. 5). In this case, the purely magnetic elastic differential SANS cross-section $d\Sigma/d\Omega$ (for unpolarized neutrons) of a bulk ferromagnet can be expressed as[15]

$$\frac{d\Sigma}{d\Omega}(\mathbf{q}) = \frac{8\pi^3}{V} b_H^2 [|\tilde{M}_x|^2 + |\tilde{M}_y|^2 \cos^2\theta + |\tilde{M}_z|^2 \sin^2\theta - (\tilde{M}_y \tilde{M}_z^* + \tilde{M}_z \tilde{M}_y^*) \cdot \sin\theta \cos\theta]. \quad (10)$$

Here, V is the scattering volume (in our simulations, a rectangular prism with $125 \times 380 \times 380\,\text{nm}^3$ and with the short side along the neutron beam, as in Fig. 5), $b_H = 2.699 \times 10^{-15}$ m/μ_B (μ_B is the Bohr magneton), a^* denotes a quantity complex conjugated to a, θ is the angle between the external field **H** and the scattering vector $\mathbf{q} = (0, q \cdot \sin\theta, q \cdot \cos\theta)$, and $\tilde{\mathbf{M}}(\mathbf{q}) = [\tilde{M}_x(\mathbf{q}), \tilde{M}_y(\mathbf{q}), \tilde{M}_z(\mathbf{q})]$ is the Fourier transform of the magnetization $\mathbf{M}(\mathbf{x})$. The relative contributions of the different terms (squared magnetization projections and mixed terms $\propto \tilde{M}_y \tilde{M}_z$) to the total cross-section in Eq. (10) are discussed in detail elsewhere.

In Eq. (10), we ignored the *nuclear* SANS contribution, because the present study is devoted to simulations of *magnetic* SANS. For samples with a statistically isotropic microstructure, nuclear coherent scattering is also isotropic and independent of the applied magnetic field. Even more importantly, the magnetic scattering that is relevant here, because of static spin misalignment, is generally several orders of magnitude larger than the nuclear SANS signal (cf. Figs. 10, 11, 18, 22, 35, and 36 in Ref. 15). Therefore, the simulated cross-section computed using Eq. (10) can be directly compared to experimental SANS data on nanocrystalline magnetic materials.

The Fourier components of the magnetization distribution for a disordered system can be calculated in the most efficient way by mapping (interpolating) this distribution onto a regular grid. We used the following method: if the center of the regular grid element (j,k,l) is inside the ith finite element of our disordered system and this element represents the hard phase fraction, the corresponding magnetic moment is calculated as

$$\mathbf{M}_{jkl}^{\text{hard}} = \frac{\mathbf{m}_i M_{S,i} V_i}{N_i^{\text{hard}}},$$

where N_i^{hard} is the number of regular grid elements whose centers are within the ith hard phase mesh element of the initial disordered system. If the center of the regular grid element is inside the soft phase, its magnetic moment is

$$\mathbf{M}_{\text{soft}}^{jkl} = \frac{\mathbf{m}_i M_{S,i} V_i}{\langle N^{\text{soft}} \rangle},$$

where $\langle N^{\text{soft}} \rangle$ is the *average* number of regular grid elements inside the finite elements used for the discretization of the soft phase. Use of the average number $\langle N^{\text{soft}} \rangle$ instead of the number N_i^{soft} of regular elements belonging to the ith finite element helps suppress nonphysical fluctuations of the magnetization distribution that arise because of significant fluctuations of N_i^{soft} for different finite elements (for computing the Fourier transform of the magnetization, we use the regular mesh that is only about two times finer than the size of a soft phase element of the initial disordered mesh). Corresponding averaging of the number of regular grid elements for the hard phase is not necessary, because each hard phase polyhedron includes a relatively large number of regular grid nodes.

Numerical results for the SANS cross-section obtained by evaluating the expression in Eq. (10) using the algorithm outlined previously are presented in Fig. 6 (lower row of images), together with the experimental results reported in Ref. 18. Both numerical and experimental pictures represent so-called difference-intensity data;[18] i.e., they are obtained by subtracting the SANS cross-section in the saturated magnetization state from the cross-section obtained at each particular field. Numerical images were averaged over eight random realizations of the nanocomposite microstructure.

Clearly, Fig. 6 demonstrates good semiquantitative agreement between experimental and numerical results, including their dependencies on the external magnetic field, which is applied in the horizontal direction with respect to the images. At zero field, the total (i.e., without subtracting the cross-section at saturation) scattering intensity is isotropic (not shown here, see Ref. 54 for details). The scattering intensity at saturation—which is used to calculate the difference-intensity images shown in Fig. 6—exhibits the angular dependence $\sim\sin^2\theta$, in agreement with Eq. (10): at saturation, $M_x = M_y = 0$ and $M_z = M_S$, so the only remaining term in Eq. (10) is $\sim\sin^2\theta$.

However, at intermediate fields (see the image for $H = 2.9$ kOe), the SANS intensity shows a nontrivial angular anisotropy in a clover-leaf shape, first observed experimentally in Ref. 29. The qualitative explanation of this effect is based on the magnetization jump at the boundary between the hard

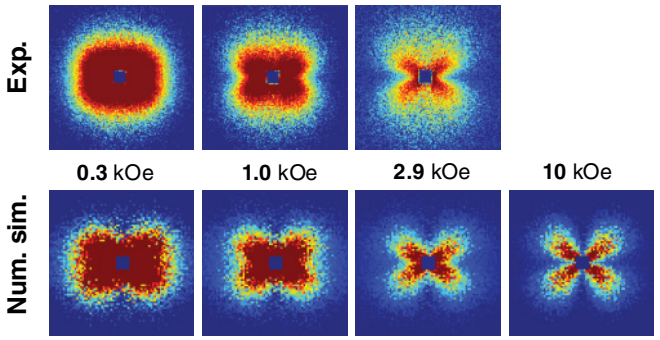

FIG. 6. (Color online) Comparison of the SANS intensities obtained experimentally (Exp., upper row) and simulated numerically (Num. sim., lower row) for different external fields as indicated (a logarithmic scale for the intensities was used). Color scales for experimental and simulated images coincide up to the scaling factor used for the normalization. Pixels in the corners of the images have a momentum transfer $q = 0.64$ nm^{-1}. The external field is applied horizontally in the plane. Experimental data were taken from Ref. 18.

and the soft phases, as discussed in Ref. 18. According to this explanation, the magnetodipolar field, arising because of this jump around the hard inclusions, leads to deviation of the magnetization direction in the amorphous phase from the external field direction. The angular dependence of this deviation is similar to the corresponding dependence of the stray field created by the hard inclusion ($\sim\sin\theta\ \cos\theta$) and introduces an additional angular dependence into the SANS intensity via $\tilde{M}_x(\mathbf{q}), \tilde{M}_y(\mathbf{q}), \tilde{M}_z(\mathbf{q})$. This additional dependence is superimposed onto the trigonometric functions of θ present in Eq. (10), leading to substantial deviations of the intensity maxima locations from their trivial values $\theta = \pm 45^{\circ}$ (for $H = 2.9$ kOe, the SANS image shown in Fig. 6 exhibits intensity maxima at $\theta \approx \pm 35^{\circ}$).

To check this explanation, we performed simulations for the same system as discussed previously but neglected the magnetodipolar interaction (i.e., the corresponding energy and effective field contributions were "switched off"). The main result of this simulation is shown in Fig. 7, where we compare the angular dependencies of the $|\tilde{M}_y(\mathbf{q})|^2$ component (computed for both systems at the same magnetization value in the applied field direction) for the system with [Fig. 7(a)] and without [Fig. 7(b)] the magnetodipolar interaction.

For the system where the magnetodipolar interaction is present, the typical clover-leaf-type pattern can be clearly seen in $|\tilde{M}_y(\mathbf{q})|^2$; for certain q and H, it delivers the main contribution to the corresponding pattern present in the total SANS cross-section. On the other hand, when the magnetodipolar interaction is neglected, this pattern disappears, thus verifying that this interaction is the main reason for the presence of the clover-leaf structure in SANS images. In magnetic nanocomposites, the internal dipolar field is mainly due to different magnetization values of the hard and soft phases, which results in significant "surface magnetic charges" on the border between these phases. These charges, in turn, induce a significant stray field. Hence, the results presented here can be considered as supporting the conclusion from Ref. 18 that the clover-leaf pattern observed in SANS is due to the magnetization jump on the border between the two magnetic phases.

V. CONCLUSION AND OUTLOOK

We have introduced a new micromagnetic methodology that is especially suitable for numerical simulations of widely used many-phase magnetic nanocomposites consisting of magnetically soft and hard phases, where the hard phase inclusions have an approximately spherical shape. By applying this new approach to the simulations of magnetization distribution and subsequent calculations of the SANS cross-sections of nanocomposites of the Nanoperm type, we could achieve good agreement with experimental data obtained on these alloys. Our preliminary studies of the role of the various magnetic interactions in this highly nontrivial material confirm that the qualitatively new clover-leaf shape seen in

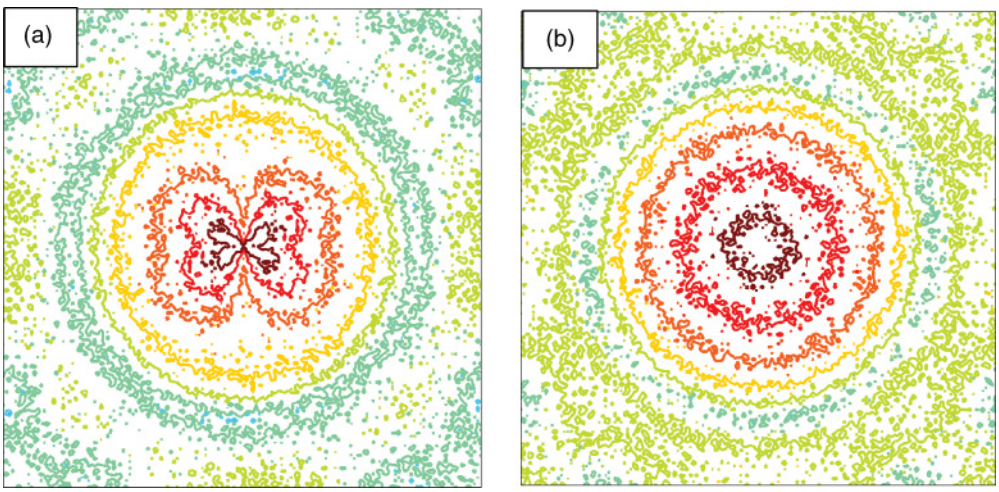

FIG. 7. (Color online) Comparison of the angular dependencies of the Fourier component $|\tilde{M}_y(\mathbf{q})|^2$ for systems (a) where the magnetodipolar interaction is taken into account and (b) where it is neglected in the applied field $H = 2.9$ kOe. For the system without the magnetodipolar interaction in (b), the clover-leaf-type pattern seen in (a) is absent and the angular dependence of $|\tilde{M}_y(\mathbf{q})|^2$ is fully isotropic.

experimental SANS data appears due to the magnetodipolar field within a nanocomposite, as previously suggested in Ref. 18. The important question of whether the abrupt jump in magnetization magnitude at the boundaries between hard and soft magnetic phases present in two-phase composites is a necessary condition for the observation of such a clover-leaf pattern will be addressed in detail in a separate publication.

ACKNOWLEDGMENTS

This work was supported by the Deutsche Forschungsgemeinschaft under the Project No. BE 2464/10-1 and by the National Research Fund of Luxembourg in the framework of ATTRACT Project No. FNR/A09/01 and Project No. FNR/10/AM2c/39.

*db@innovent-jena.de

[1] G. Herzer, in *Handbook of Magnetic Materials*, edited by K. H. J. Buschow (Elsevier, Amsterdam, 1997), Vol. 10, pp. 415.
[2] J. J. Croat, J. F. Herbst, R. W. Lee, and F. E. Pinkerton, J. Appl. Phys. **55**, 2078 (1984).
[3] R. Coehoorn, D. B. de Mooij, J. P. W. B. Duchateau, and K. H. J. Buschow, J. Phys., **49**, C8-669 (1988).
[4] E. F. Kneller and R. Hawig, IEEE Trans. Magn. **27**, 3588 (1991).
[5] L. Schultz and K.-H. Müller (eds.), *Magnetic Anisotropy and Coercivity in Rare-Earth Transition Metal Alloys* (Werkstoff-Informationsgesellschaft, Frankfurt, 1998).
[6] M. E. McHenry, M. A. Willard, and D. E. Laughlin, Prog. Mater. Sci., **44**, 291 (1999).
[7] K. Suzuki and G. Herzer, in *Advanced Magnetic Nanostructures*, edited by D. Sellmyer and R. Skomski (Springer, New York, 2006), p. 365.
[8] A. Hubert and R. Schäfer, *Magnetic Domains* (Springer-Verlag, Berlin, 1998).
[9] U. Hartmann, Ann. Rev. Mater. Sci. **29**, 53 (1999).
[10] R. Wiesendanger, *Scanning Probe Microscopy and Spectroscopy* (Cambridge University Press, Cambridge, UK, 1994).
[11] M. Bode, Rep. Prog. Phys. **66**, 523 (2003).
[12] E. Bauer, J. Phys. Cond. Matt. **13**, 11391 (2001).
[13] A. Wiedenmann, Phys. B **356**, 246 (2005).
[14] W. Wagner and J. Kohlbrecher, in *Modern Techniques for Characterizing Magnetic Materials*, edited by Y. Zhu (Kluwer Academic Publishers, Boston, 2005), pp. 65.
[15] A. Michels and J. Weissmüller, Rep. Prog. Phys. **71**, 066501 (2008).
[16] W. Schmatz, T. Springer, J. Schelten, and K. Ibel, J. Appl. Crystallogr. **7**, 96 (1974).
[17] V. Gerold and G. Kostorz, J. Appl. Crystallogr. **11**, 376 (1978).
[18] A. Michels, C. Vecchini, O. Moze, K. Suzuki, P. K. Pranzas, J. Kohlbrecher, and J. Weissmüller, Phys. Rev. B **74**, 134407 (2006).
[19] A. Michels, Phys. Rev. B **82**, 024433 (2010).
[20] A. Bracchi, K. Samwer, S. Schneider, and J. F. Löffler, Appl. Phys. Lett. **82**, 721 (2003).
[21] E. García-Matres, A. Wiedenmann, G. Kumar, J. Eckert, H. Hermann, and L. Schultz, Phys. B **350**, 315E (2004).
[22] A. Danzig, A. Wiedenmann, and N. Mattern, J. Phys. Cond. Matt. **10**, 5267 (1998).
[23] H. Hermann, A. Heinemann, N. Mattern, and A. Wiedenmann, Europhys. Lett. **51**, 127 (2000).
[24] A. Heinemann, H. Hermann, A. Wiedenmann, N. Mattern, and K. Wetzig, J. Appl. Crystallogr. **33**, 1386 (2000).
[25] A. Wiedenmann, Phys. B **297**, 226 (2001).
[26] J. Kohlbrecher, A. Wiedenmann, and H. Wollenberger, Z. Phys. B **104**, 1 (1997).
[27] A. Michels, R. N. Viswanath, and J. Weissmüller, Europhys. Lett. **64**, 43 (2003).
[28] A. Grob, S. Saranu, U. Herr, A. Michels, R. N. Viswanath, and J. Weissmüller, Phys. Stat. Sol. A, **201**, 3354 (2004).
[29] A. Michels, C. Vecchini, O. Moze, K. Suzuki, J. M. Cadogan, P. K. Pranzas, and J. Weissmüller, Europhys. Lett. **72**, 249 (2005).
[30] C. Vecchini, O. Moze, K. Suzuki, P. K. Pranzas, J. Weissmüller, and A. Michels, Appl. Phys. Lett. **87**, 202509 (2005).
[31] A. Guinier and G. Fournet, *Small-Angle Scattering of X-Rays* (Wiley, New York, 1955); O. Glatter and O. Kratky (eds.), *Small-Angle X-Ray Scattering* (Academic Press, London, 1982); L. A. Feigin and D. I. Svergun, *Structure Analysis by Small-Angle X-Ray and Neutron Scattering* (Plenum Press, New York, 1987); S.-H. Chen and T. L. Lin, in *Methods of Experimental Physics-Neutron Scattering*, edited by D. L. Price and K. Sköld (Academic Press, San Diego, 1987), Vol. 23B, pp. 489–543; P. Lindner and Th. Zemb (eds.), *Neutron, X-Ray and Light Scattering: Introduction to an Investigative Tool for Colloidal and Polymeric Systems* (Elsevier, Amsterdam, 1991); J. S. Pedersen, in *Neutrons, X-Rays and Light: Scattering Methods Applied to Soft Condensed Matter*, edited by P. Lindner and Th. Zemb (Elsevier, Amsterdam, 2002), p. 391; D. I. Svergun and M. H. J. Koch, Rep. Prog. Phys. **66**, 1735 (2003); H. B. Stuhrmann, *ibid.* **67**, 1073 (2004); Y. B. Melnichenko and G. D. Wignall, J. Appl. Phys. **102**, 021101 (2007).
[32] W. F. Brown Jr., *Micromagnetics* (Interscience Publishers, New York, 1963).
[33] A. Aharoni, *Introduction to the Theory of Ferromagnetism* (Clarendon Press, Oxford, 1996).
[34] H. Kronmüller and M. Fähnle, *Micromagnetism and the Microstructure of Ferromagnetic Solids* (Cambridge University Press, Cambridge, UK, 2003).
[35] H. Kronmüller, A. Seeger, and M. Wilkens, Z. Phys. **171**, 291 (1963).
[36] J. F. Löffler, H. B. Braun, W. Wagner, G. Kostorz, and A. Wiedenmann, Phys. Rev. B **71**, 134410 (2005).
[37] M. Donahue and D. Porter [http://math.nist.gov/oommf/].
[38] M. Scheinfein [http://llgmicro.home.mindspring.com/].
[39] D. V. Berkov and N. L. Gorn, [http://www.micromagus.de].
[40] A. Vansteenkiste and B. Van de Wiele, J. Magn. Magn. Mater **323**, 2585 (2011).
[41] F. Y. Ogrin, S. L. Lee, M. Wismayer, T. Thomson, C. D. Dewhurst, R. Cubitt, and S. M. Weekes, J. Appl. Phys. **99**, 08G912 (2006).
[42] S. Saranu, A. Grob, J. Weissmüller, and U. Herr, Phys. Stat. Sol. A **205**, 1774 (2008).
[43] H. Fukunaga, N. Kitajima, and Y. Kanai, Mater. Trans. **37**, 864 (1996).
[44] R. Fischer and H. Kronmüller, Phys. Rev. B **54**, 7284 (1996).
[45] R. Fischer, T. Leineweber, and H. Kronmüller, Phys. Rev. B **57**, 10723 (1998).
[46] H. Kronmüller, S. Parkin (eds.), *Handbook of Magnetism and Advanced Magnetic Materials* (John Wiley & Sons, Chichester, UK, 2007), Vol. 2, pp. 795.

[47]J. Fidler, P. Speckmayer, T. Schrefl, and D. Suess, J. Appl. Phys. **97**, 10E508 (2005).

[48]W. S. Jodrey and E. M. Tory, Phys. Rev. A **32**, 2347 (1985).

[49]D. V. Berkov and N. L. Gorn, in *Handbook of Advanced Magnetic Materials*, edited by Y. Liu, D. Shindo, and D. J. Sellmyer (Springer Verlag and Tsinghua University Press, ISBN 7-302-08701-6/T, 2005), Vol. 2, pp. 421–507.

[50]P. Gibbon and G. Sutmann, in *Quantum Simulations of Complex Many-Body Systems: From Theory to Algorithms, Lecture Notes*, edited by J. Grotendorst, D. Marx, and A. Muramatsu, (John von Neumann Institute for Computing, Julich, NIC Series, ISBN 3-00-009057-6, 2002), Vol. 10, pp. 467–506.

[51]D. V. Berkov and N. L. Gorn, Phys. Rev. B **57**, 14332 (1998).

[52]N. L. Gorn, D. V. Berkov, P. Görnert, and D. Stock, J. Magn. Magn. Mat. **310**, 2829 (2007).

[53]M. Deserno and C. Holm, J. Chem. Phys. **109**, 7678 (1998).

[54]S. Erokhin, D. Berkov, N. Gorn, and A. Michels, IEEE Trans. Magn. **47**, 3044 (2011).

[55]K. Suzuki and J. M. Cadogan, Phys. Rev. B, **58**, 2730 (1998).

[56]K.-H. Hellwege and O. Madelung (eds.), *Landolt-Börnstein: Numerical Data and Functional Relationships in Science and Technology* (Springer-Verlag, Berlin-Heidelberg, 1986), Vol. 19a, p. 74.